Effect of Freeze/Thaw on Aggregation and Transport of nano-TiO_2 in Saturated Porous Media

Jeffrey M. Farner*, Jacopo De Tommaso, Heather Mantel, Rachel S. Cheong, Nathalie Tufenkji

Department of Chemical Engineering, McGill University, Montreal, Quebec, Canada

*Corresponding Author Phone: (514) 398-4494; Fax: (514) 398-6678; E-mail: jeffrey.farner@mcgill.ca

Environmental Significance Statement

The effect of winter conditions on the environmental fate of titanium dioxide nanoparticle (TiO_2 NP) suspensions remains unexplored. This work compares the impact of a 24 h freeze/thaw cycle to suspensions of TiO_2 held at 10 °C for 24 h in environmentally relevant water chemistries to mimic winter conditions in locations where daytime temperatures rise above freezing while nighttime temperatures drop below freezing. Exposure to a freeze/thaw cycle increases the size of aggregates, suspension polydispersity, and deposition in the column. Furthermore, inherent differences between two formulations of TiO_2 NPs lead to suspensions with dissimilar aggregate sizes and stabilities for the same water chemistry. This work demonstrates that exposure to freezing temperatures will significantly impact particle stability and transport.

TOC Art

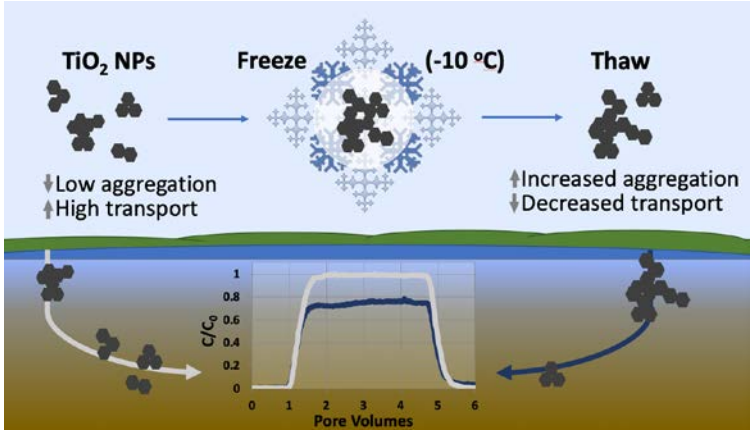

Novelty of the work

This work demonstrates that exposing TiO_2 nanoparticle suspensions to freezing temperatures induces aggregation and impacts transport in model groundwaters.

Abstract

Extensive research has been conducted on nanoparticle (NP) aggregation and transport behavior in saturated granular porous media, but few studies to date have looked at the effect that temperature variability associated with winter conditions will have on engineered NPs. To investigate the effect of these fluctuations above and below freezing on particle stability, titanium dioxide (TiO_2) NPs were subjected to a freeze/thaw (FT) cycle, which led to aggregation and increased deposition in a saturated granular porous medium. We compare NP aggregation and transport behavior for two commercially available formulations of TiO_2, which exhibited differences in aggregation in suspension and deposition to a quartz sand. A single FT cycle induced TiO_2 aggregation, increased the heterogeneity of aggregate sizes, and increased deposition in a saturated porous media. Nanoparticles subjected to FT in the presence of organic matter underwent greater aggregation and deposition relative to NPs held at 10 °C. Calculations of attachment efficiency for a given amount of deposition are shown to depend on aggregate size, highlighting a limitation in assigning a single value for the attachment efficiency in polydisperse samples. This study suggests that NP behavior and transport in cold weather climates will differ from warmer environments and that the increased cycling of freezing and thawing associated with climate change will further influence the fate of NPs.

1. Introduction

Titanium dioxide (TiO_2) NPs are increasingly employed in consumer products due in part to their white pigmentation and ability to absorb UV radiation (1, 2), and up to 45% of the commercial TiO_2 NP market is used by the coatings industry (3). When applied as additives to construction material such as cement or exterior paint, nanoparticles (NPs) are subject to natural weather and potential release (4-8). In a related study, freeze and thaw cycles were observed to induce TiO_2 NP release from painted surfaces (9). As a result of their use, disposal, or unintended release, TiO_2 NPs will make their way into the environment. Differences in aggregate stability and photoreactivity have been observed for different TiO_2 formulations which suggests that inherent properties of the particles will influence TiO_2 behavior in the environment (10). Anticipated environmental concentrations for TiO_2 in freshwater range widely, with concentrations from less than one to hundreds of ng/L (1, 11-15).

In the environment, NPs will interact with suspended colloids and organic matter in surface waters and the surfaces of granular media in riverbanks or groundwater (16-19). Understanding the parameters that govern or affect aggregate behavior is critical to understanding fate and transport of NPs in the environment (20-22). For example, the impact of natural organic matter (NOM) on NP stability is not always straightforward (23). Humic acid has been shown to limit TiO_2 aggregation and deposition due to steric repulsion (24), although in the presence of Ca^{2+}, NOM can also lead to bridging (25-27). Column tests are commonly used to investigate the influence of both ionic strength (IS) and NP coating on TiO_2 NP deposition and attachment (20, 28-31).

In many climates, the repeated cycles of freezing and thawing present a largely unexplored phenomenon. Freeze/thaw (FT) cycling in soils has been linked to changes in nutrient cycling and soil properties (32, 33) as well as variations in bacterial transport and virulence in the environment (34-37). As the global climate changes, the frequency of annual soil FT cycles in northern locations is increasing, and this trend is projected to continue (38). FT cycles have been shown to induce the generation of colloids from soils and mobilize soil-associated metals such as cesium and strontium (39). Gold, graphene oxide, and latex NPs have shown freezing-related aggregation as particles are excluded from the ordering water molecules and formation of ice crystals during the freezing process, increasing both the local particle concentration and ionic strength in the still-unfrozen water (40-44). The ease with which freeze-dried gold nanoparticles were reconstituted was shown to depend on the attachment of a NP stabilizing agent; mercaptoacetic acid, which was strongly chemisorbed, was much more effective than weakly physisorbed citrate at preventing irreversible aggregation (42). This was ascribed to the weak interactions between citrate and the surface being overcome by the stresses associated with solute exclusion and freezing. However, no literature has been published on the effect of FT on TiO_2 NPs. Furthermore, how porewater ionic strength or the presence of natural organic macromolecules affect these temperature-dependent behaviors remains unexplored.

In this work, we subjected TiO_2 NPs to two different 24 h temperature pre-treatments: suspensions either were held at 10 °C or underwent a FT cycle. We hypothesized that subjecting suspensions to a FT cycle would result in NP aggregation and lead to increased

particle retention in saturated granular porous media. FT samples were compared to those held for 24 h at 10 °C, and these results are compared to the aggregation and transport behaviors of two different commercial formulations of TiO_2 that were measured at 10 °C without any pre-treatment. Nanoparticle transport and deposition were measured as a function of ionic strength and concentration of natural organic matter. Inherent differences between NP formulations resulted in suspensions with dissimilar stabilities and aggregate sizes for the same water chemistry. Lastly, as FT is observed to induce aggregation, the impact of suspension polydispersity on calculations of attachment efficiency is investigated.

2. **Materials and Methods**

2.1. TiO_2 Nanoparticles

Experiments were performed with two sources of TiO_2. The first, P25 Aeroxide (Evonik, Germany), is a mixture of 25 nm primary particles composed of anatase and rutile at roughly an 80/20 ratio, respectively. The second TiO_2 NP (CoRI) is a proprietary formulation used as a paint additive and obtained from the Coatings Research Institute (CoRI, Belgium). CoRI is composed of 5-15 nm primary particles of 95+ % anatase. Both particles were previously characterized (10). Stock TiO_2 suspensions were prepared at 100 mg/L in deionized water (DI). Immediately prior to use, stock suspensions were probe sonicated (Q700, QSonica, Newton, CT, USA) for 6 minutes in pulse mode (12 s on, 3 s off) following the NIST protocol by Taurozzi *et al.* (45). All experiments and characterization measurements were performed using 5 ppm TiO_2 suspensions.

The aggregate size of TiO_2 suspensions was determined by dynamic light scattering (DLS) using a Zetasizer Nano ZS (Malvern Panalytical). Size measurements are reported both as intensity weighted hydrodynamic diameter and Z-average diameter (cumulants mean diameter) as determined by the instrument software. The polydispersity index (PDI), which ranges from 0 (monodisperse) to 1 (highly polydisperse), returns the normalized standard deviation of a gaussian distribution of the monomodal fit of the cumulant analysis (Z-average) and therefore gives useful information about the width of the peak and the polydispersity of the sample (46). The inclusion of PDI when reporting size from DLS is suggested by the US National Institute of Standards and Technology (47). For polydisperse samples, differences between Z-average and intensity weighted diameters arise from how the Zetasizer software calculates size from the autocorrelation function. The Z-Average and PDI values are calculated using the cumulant fit plot to yield a single average size and a descriptor of the polydispersity (48). The intensity weighted diameter is calculated using the distribution analysis, which includes longer times and will return multiple results for polydisperse data in order to minimize the cumulant residual. In polydisperse samples, the effect is that the intensity weighted diameter reduces the influence of the largest aggregates, though it should be noted that DLS results of highly polydisperse samples generally do not meet the instrument quality criteria (49-51). Aggregate morphology and primary particles were visualized using transmission electronic microscopy (TEM), (Philips CM200 TEM, Advanced Microscopy Techniques Corp.). TEM was performed on suspensions deposited onto lacey carbon grids and allowed to dry at room temperature. Electrophoretic mobility (EPM) measurements were collected via Zetasizer and converted to Zeta Potential (ZP) via the Henry equation using the Smulochowski approximation for a thin double layer. Scanning

electron microscopy (SEM) was performed on aggregates drop-cast and dried on silicon wafers and coated with a 3 nm layer of platinum (Leica Microsystems EM ACE600 sputter coater). Imaging was performed using a FEI Quanta 450 environmental SEM.

2.2. Solution Chemistry

Stock natural organic matter (NOM) solutions (100 mg/L) were prepared in either DI water or Moderately Hard Reconstituted Water (MHRW) using Suwannee River NOM, Reverse Osmosis Isolate (International Humic Substances Society, USA). The solutions were pH adjusted to 7.9 with NaOH and stirred overnight. Natural organic matter stock solutions were covered in aluminum foil and stored at 4 °C prior to use when they were diluted to final concentrations of 1 - 10 mg/L. Moderately hard reconstituted water, consisting of 96 mg/L sodium bicarbonate (99.7+%, Sigma-Aldrich), 60 mg/L calcium sulfate dehydrate (98%, Arcos Organics), 60 mg/L magnesium sulfate (Fisher Scientific), and 4 mg/L potassium chloride (USP, Fisher Scientific) was prepared in the laboratory. The resulting water is designed to produce a standard, moderately hard water with an ionic strength of 13 mM, pH of 7.4 - 7.8, hardness of 80 - 100 mg $CaCO_3$/L, and alkalinity of 60 - 70 mg $CaCO_3$/L (52). Test suspensions were made by adding freshly prepared stock TiO_2 to a solution of NOM and either sodium chloride (ACS grade, Fisher Scientific) or MHRW which had been previously prepared and stored overnight at 10 °C. These were adjusted to pH = 7.9 ± 0.1 with NaOH and HCl prior to each run.

2.3. Freeze/Thaw Cycles

To simulate the temperature conditions during winter shoulder periods and to observe the effect of freezing, suspensions were subjected to a FT cycle lasting 24 h, as shown in Figure S1. During a FT cycle, the temperature was brought from +10 to -10 °C over 8 h, held at -10 °C for 4 h, brought back to +10 °C over 8 h, and then held at 10 °C for 4 h. Temperature ramps were performed in a recirculating chiller (Julabo 200F) filled with a 70/30 ratio of water/propylene glycol. All particle suspensions used in FT studies were prepared in the same manner as described above, with 100 mL samples evenly split into three 50 mL centrifuge tubes, sealed with parafilm, and placed in the chiller for 24 h. Prior to each transport experiment, sample tubes were gently inverted by hand to resuspend settled aggregates while minimizing their break-up.

2.4. Column Tests

All column experiments were conducted at 10 °C using 5 ppm TiO_2 suspensions. Column tests were performed on three types of samples: suspensions freshly prepared and run immediately (labeled as t0), suspensions subjected to a 24 h FT cycle (labeled as FT), and suspensions held for 24 h at 10 °C before running (labeled as 10C). Values reported are the average of duplicate runs. Figure S2 presents a schematic of the column test setup. To reduce the size of the aggregates, test suspensions of CoRI NPs were sonicated a second time after dilution and prior to analysis using the same sonication procedure as for the stock TiO_2 suspensions. For column tests, 26 g of high purity quartz sand (-50 +70 mesh size, d_{50} = 256 µm, density = 2.6 g/cm^3, Sigma-Aldrich) which had been previously cleaned following the method employed by Pelley and Tufenkji (53) was soaked in electrolyte and stored overnight in the fridge at 10 °C. Glass columns (8.5 cm packed length, 1.6 cm internal diameter) were

wet packed and the porous medium was supported on a Nylon Spectra/Mesh filter (pore size: 70 μm, thickness: 70 μm) to prevent sand from exiting the column. Columns were packed using vibration to prevent air being trapped and to ensure uniform packing. One pore volume (PV) was calculated as the difference between the total volume of the packed column and the volume of the sand used (mass of sand divided by density). This was confirmed using 0.01 M KNO_3 as a tracer and measuring the time necessary for the tracer in the effluent to reach 50% of the influent concentration. Multiplying this time by the injection rate (0.9 mL/min) gave a value of 1 PV = 7.29 mL. The column porosity, calculated as one PV divided by the total volume of the packed column, was 0.43. Columns were equilibrated by passing at least 12 PVs of electrolyte through the bed via syringe pumps (Kd Scientific) at a constant approach (superficial) velocity of 7.5×10^{-5} m/s. After equilibration, 3.7 PVs of NP suspension were introduced into the column. Column effluent (C) was monitored with UV-Vis spectrophotometry (Agilent 8453) at 270 nm using a 1 cm flow cell (Agilent). Bypassing the column provided the absorbance of influent particles (C_0). Tubes and columns were rinsed thoroughly after each test with 0.1 M NaOH, followed by copious amounts of DI and air-dried. Breakthrough curves (BTCs), indicating the NP concentration in the effluent over time, were plotted as C/C_0 versus PV. Column bypass controls were performed with suspensions of TiO_2 in the absence of NOM in MHRW (i.e., conditions in which significant particle deposition is anticipated). Measuring the absorbance of the suspension over the duration of the column test while bypassing the column indicated stable absorbance readings (data not shown), suggesting that any aggregation that may have occurred during the column tests was either insignificant or did not appreciably alter absorbance values.

2.5. Nanoparticle-Collector Attachment Efficiency and Single-Collector Contact Efficiency

Attachment efficiencies were calculated using data from absorbance measurements and DLS according to the Tufenkji and Elimelech equation (29):

$$\alpha = -\frac{2\,d_c}{3\,(1-\varepsilon)\,L\,\eta_0}\ln\left(\frac{C}{C_0}\right) \qquad \text{Eq. 1}$$

where α is the attachment efficiency, d_c is the collector diameter, ε is the porosity, L is column length, η_0 is the calculated single-collector contact efficiency, and C/C_0 is the normalized absorbance data from the column output. The single-collector contact efficiency depends on aggregate size and is the summation of three different mechanisms, namely, diffusion due to Brownian motion (η_D), interception from the fluid transport (η_I), and gravity (η_G). A detailed explanation can be found in Tufenkji and Elimelech, 2004 (29). Because both NPs are primarily anatase (P25 consists of ~20% rutile) and little difference is observed between anatase and rutile in reported Hamaker constant values of A_{121} (22, 54), the same Hamaker constant ($A_{TiO_2-H_2O-SiO_2}$ = 1.4 × 10^{-20} J) was used for both P25 and CoRI in η_0 calculations (55, 56).

3. Results and Discussion

3.1. Nanoparticle Characterization

The ZP of NP suspensions was measured for each of the water chemistries studied (Table 1, Figure 1a and 1d). Broadly, the surface charge of P25 and CoRI NPs are similar. Zeta potential was more significantly impacted by changes in IS than the addition of NOM. Nanoparticles were negatively charged for all conditions as expected given that the pH used (7.9) is higher

than the PZC for TiO_2 (~ 6.3) (57). The presence of divalent cations in MHRW compressed the electrical double layer and destabilized NPs, resulting in calculated ZP values much closer to those observed in 100 mM NaCl, despite the ionic strength (13 mM) being more similar to 10 mM NaCl. In previous characterization, X-ray photoelectron spectroscopy did not indicate the presence of capping agents or surface passivation for either TiO_2 NP (10).

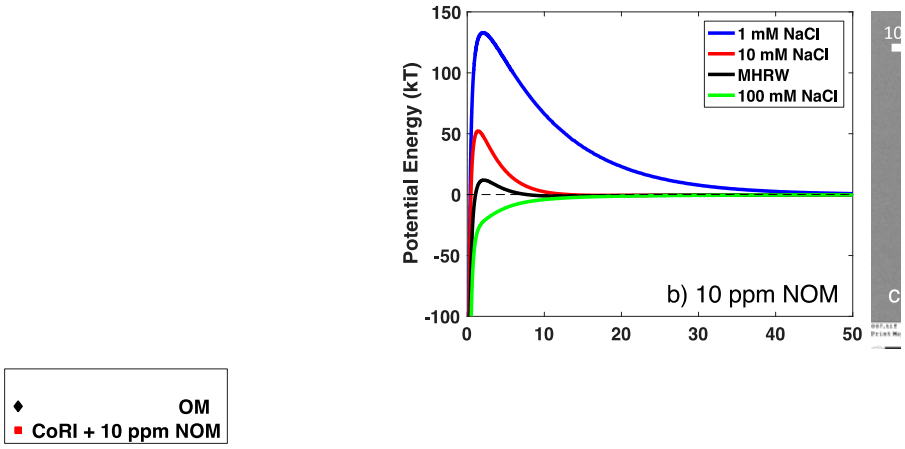

Figure 1. NP Characterization. ZP of TiO_2 as a function of IS and NOM concentration for a) P25 NPs and d) CoRI NPs. Error bars in indicate standard deviation (n=3). XDLVO calculations of TiO_2 interaction with SiO_2 b) in 10 ppm NOM as a function of IS and e) in 10 mM NaCl as a function of NOM concentration. TEM of c) P25 and f) CoRI aggregates following suspension in MHRW. Values for XDLVO calculations are presented in Table S3. The data at 13 mM IS represent experiments conducted with MHRW.

Calculations of particle interactions with a SiO_2 surface using extended DLVO (XDLVO) theory were performed using the Micro- and Nanoparticle transport, filtration and clogging Model – Suite (MNMs 2018 version 3.010). Interaction profiles are shown in Figures 1b and

1e for the TiO_2 – H_2O – SiO_2 system for suspensions of TiO_2. The XDLVO profiles shown consider steric interactions (osmotic and elastic repulsion) in addition to the electrical and double layer interactions of traditional DLVO theory (58, 59). The osmotic repulsion represents the forces generated by compression of the brush layer when the colloidal particles approach each other, while the elastic repulsion is an additional hindrance due to the polymeric chains absorbed on the particle surface (23). Further details about XDLVO calculations are given in the Supporting Information (Table S3). Given that our system uses non-spherical particles in a complex media, these calculations should be considered rough estimates only, however XDLVO calculations for the increasing IS series of P25 NPs in 10 ppm NOM (Figure 1b) suggest that a barrier to deposition exists for 1 mM NaCl, 10 mM NaCl, and MHRW but not for 100 mM NaCl.

Table 1 presents the suspension characteristics for conditions that were prepared and run immediately (t0). Suspensions of P25 consisted of fairly small (~160 nm) and monodisperse (PDI ≤ 0.2) aggregates across the various water chemistries. P25 aggregates in the presence of NOM at 100 mM IS were slightly larger (~245 nm), but the PDI remained below 0.3. For suspensions of CoRI NPs, which produced highly polydisperse aggregates (all PDIs were greater than 0.6), there is a discrepancy between Z-average size and intensity weighted size. While the intensity weighted average diameters were on the order of a few hundreds of nm, the Z-average diameters were almost all over 1 μm, suggesting that suspensions of CoRI contain a majority of aggregates at the smaller size range (approx. 200 – 500 nm) but also a significant amount of larger aggregates (greater than 1 μm). For perfectly monodisperse samples, the Z-average and intensity weighted sizes would be the same.

Table 1. Summary of NP characterization for suspensions run immediately (t0) at 10 °C.

				Influent Aggregate Size (Diameter, nm)				Apparent α	
Suspension	**IS (mM)**	**NOM (ppm)**	**ZP (mV)**	**Z-average**	**PDI**	**Intensity Weighted**	C/C_0	**Z-average**	**Intensity Weighted**
P25, t0	1	0	-29.9 ± 1.5	165	0.19	176	0.99	0.004	0.005
		1	-29.0 ± 0.7	158	0.15	180	0.98	0.006	0.012
		10	-33.6 ± 1.5	148	0.15	188	0.98	0.006	0.002
	10	0	-24.4 ± 0.3	160	0.16	129	0.59	0.088	0.088
		1	-32.1 ± 0.2	160	0.20	170	0.95	0.010	0.010
		10	-36.2 ± 3.6	151	0.20	151	0.99	0.004	0.004
	MHRW (13)	0	-16.4 ± 0.7	153	0.18	163	0.17	0.253	0.266
		1	-20.1 ± 1.7	149	0.16	171	0.89	0.017	0.019
		10	-18.8 ± 0.8	163	0.18	163	0.97	0.014	0.014
	100	0	-19.6 ± 2.3	162	0.16	127	0.03	0.570	0.472
		1	-25.2 ± 0.6	242	0.23	242	0.36	0.212	0.212
		10	-23.3 ± 1.5	245	0.28	235	0.48	0.172	0.167
CoRI, t0	1	0	-32.9 ± 2.0	934	0.75	355	0.74	0.071	0.063
		1	-42.6 ± 2.0	833	0.61	520	0.90	0.059	0.060
		10	-38.3 ± 2.1	1044	0.75	411	0.73	0.076	0.076
	10	0	-34.5 ± 1.4	1121	0.78	404	0.48	0.190	0.200
		1	-36.5 ± 1.5	2077	0.98	201	0.57	0.070	0.103
		10	-34.3 ± 2.6	1906	0.97	250	0.72	0.040	0.061
	MHRW (13)	0	-20.1 ± 0.7	2093	1.00	192	0.35	0.162	0.235
		1	-20.7 ± 0.4	1730	0.92	341	0.59	0.100	0.161
		10	-24.2 ± 0.6	1155	0.75	436	0.77	0.079	0.089
	100	0	-18.6 ± 0.5	2532	0.87	916	0.04	0.335	1.201
		1	-20.5 ± 1.1	949	0.79	560	0.14	0.704	0.753
		10	-20.0 ± 0.8	1001	0.72	435	0.11	0.498	0.499

3.2. Transport of Freshly Prepared Suspensions at 10 °C: t0

To understand the baseline behavior of P25 and CoRI NPs, column tests were first performed at 10 °C immediately after sonication of the TiO_2 stock suspensions (t0). Broadly, C/C_0 was lower for CoRI suspensions than for P25 in the same water chemistries (representative examples shown in Figure S4). Figure 2a shows that deposition of CoRI particles decreased with increasing NOM concentration in MHRW, resulting in higher C/C_0 values. This can be attributed to electrosteric stabilization of the suspension through the addition of NOM, as ZP generally became slightly more negative with increasing NOM concentration. In Figure 2b, deposition of P25 increased with increasing IS in the presence of 10 ppm NOM. These results

are reflected in the strong decrease in C/C_0 and calculations of α, which increases nearly an order of magnitude at 100 mM NaCl (Figure 2d), and agree with the XDLVO theory calculations (Figure 1).

Calculations of attachment efficiency, α, were performed using Equation 1 for each condition using both the Z-average ($\alpha_{\text{z-avg}}$) and the intensity weighted size ($\alpha_{\text{intensity}}$). In general, these values agree well with each other, the larger Z-average size compared to intensity weighted is observed to reduce the calculated α value. This is most apparent for conditions in which the difference in sizes is large (e.g., CoRI NPs in 100 mM NaCl, 0 ppm NOM: $\alpha_{\text{z-avg}}$ = 0.335, $\alpha_{\text{intensity}}$ = 1.201). Stability curves of calculated $\alpha_{\text{intensity}}$ values versus IS are plotted for the various conditions in Figure 2c and 2d. Generally, α increases with IS and decreases in the presence of NOM for each of the TiO_2 NPs. As can be seen, the greatest differences in α values between P25 and CoRI are observed at low ionic strengths or in the presence of NOM. These correspond to more stable conditions in which differences in the behavior and aggregate formation between the two NP formulations in suspension influence transport. At 1 mM NaCl for all suspensions, α values for P25 are nearly an order of magnitude lower than those for CoRI.

As discussed above (Section 3.1), sonicating P25 produces relatively small and uniform aggregates. In contrast, aggregates of CoRI NPs are larger and more heterogeneous after sonication. Previously, CoRI NPs were observed to undergo greater homoaggregation compared to P25 in MHRW over 48 h, both in the presence and absence of NOM (10). For the larger aggregates in a polydisperse suspension, physical straining will lead to a mechanical

filtration effect, reducing C/C_0 and influencing calculations of α (28). This is anticipated when aggregate to collector diameter ratios (d_a/d_c) are greater than ~0.003 (60, 61). In this study, the quartz sand diameter of 256 µm corresponds to a critical size of straining for aggregates above ~768 nm. The BTCs shown in Figures 2a and 2b do not imply the presence of straining, which would be characterized by a decreasing C/C_0 over time (20). Instead, the shape of the BTC for CoRI in the absence of NOM (Figure 2a, blue line) is more suggestive of blocking, in which favorable deposition sites become filled during the column test, leading to greater transport over time (62, 63).

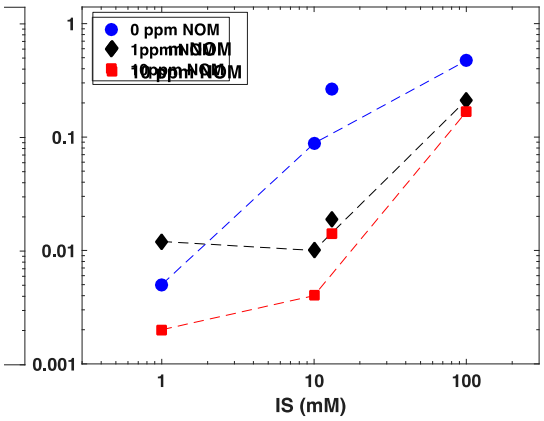

Figure 2. TiO_2 NP transport and deposition data at 10 °C. BTCs, plotted as C/C_0 versus PV, of a) CoRI in MHRW as a function of NOM concentration and b) P25 in 10 ppm NOM as a function of IS. Stability diagrams showing attachment efficiency ($\alpha_{intensity}$) versus IS as a

function of NOM concentration for c) CoRI and d) P25. The data at 13 mM IS represent experiments conducted with MHRW.

The addition of NOM at higher IS highlights the influence of steric and electrostatic stabilization on NP transport, as α values for both P25 and CoRI NPs decrease with increasing NOM concentration. In conditions in which destabilization is relatively minor and overcome by the organics (e.g., 10 mM NaCl and MHRW for 1 and 10 ppm NOM), the decrease in α is greater for P25, suggesting it is more readily stabilized than CoRI. In P25 without NOM in 10 mM NaCl and MHRW, α values are quite similar to those for CoRI. The addition of NOM stabilizes the smaller and more monodisperse P25 aggregates, leading to α values at 10 mM and in MHRW that are much lower for P25 than for CoRI. At high IS (100 mM NaCl) the compression of the electrical double layer largely outweighs any steric stabilization imparted by the NOM and thus α for the two types of NPs are much more similar.

3.3. NP Aggregation and Transport Following 24 h Temperature Pre-treatments: FT and 10C

In preliminary column tests with CoRI NPs, aggregation in both FT and 10C samples led to low absorbance measurements that yielded non-reproducible results. This is unsurprising, given the large and highly polydisperse aggregates observed even at low IS in t0 conditions. As a result, the impact of water chemistry and NOM on NP transport was not investigated further for CoRI NPs. For P25, the smaller initial aggregate sizes, less polydispersity, and greater transport in t0 column studies facilitated investigation into the impact of FT and 10C temperature pretreatments.

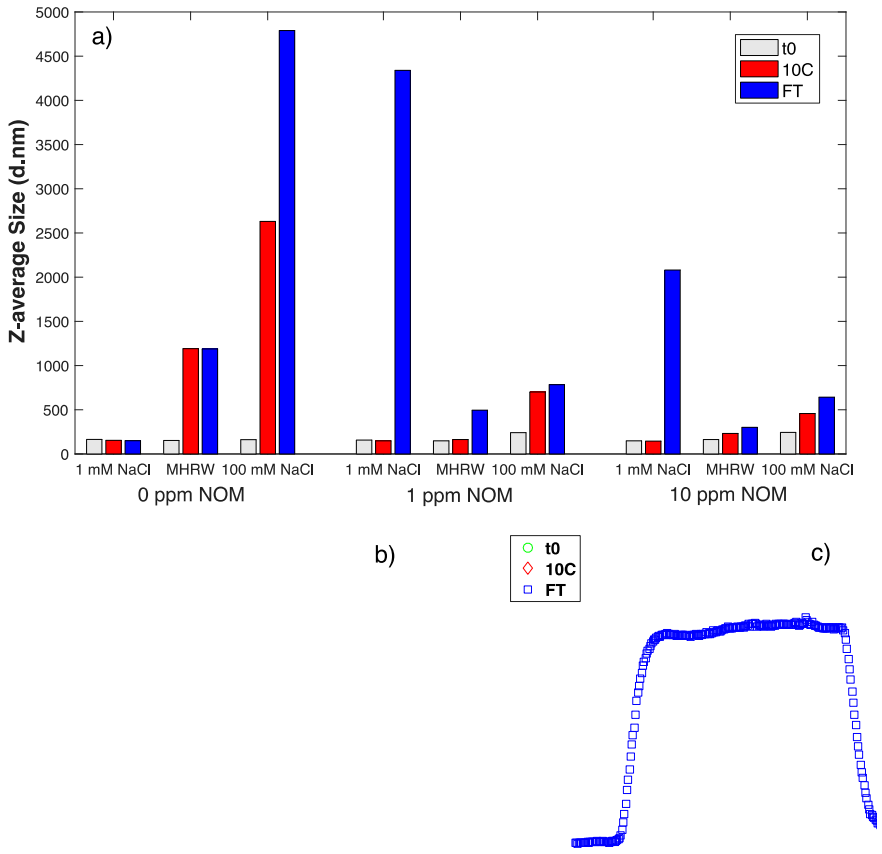

Figure 3. a) Z-average size versus water chemistry for P25 NPs as a function of temperature treatment. BTCs of b) P25 in 1 mM NaCl and 10 ppm NOM and c) P25 in MHRW and 1 ppm NOM as a function of temperature pre-treatment.

For P25, the t0 Z-average sizes are largely the same regardless of IS or NOM concentration, however in 10C samples the Z-average size is observed to increase with IS (Figure 3a, red bars). The presence of NOM has a mitigating impact, though some aggregation is still observed. This trend of increasing size with IS is largely followed for FT samples, except for suspensions in 1 mM NaCl in the presence of 1 or 10 ppm NOM, where the aggregate size is much larger than suspensions in MHRW and 100 mM NaCl. The impact of size on BTCs can be observed in Figures 3b and 3c. In 10ppm NOM and 1 mM NaCl, the Z-average size of t0

and 10C suspensions are similar (146 and 148 nm, respectively) whereas the Z-average size of FT samples is much larger (2081 nm).

The impact of freezing on aggregation has primarily been studied in terms of freeze-drying NP suspensions (40, 41, 44, 64). As water molecules in suspension become more ordered during the process of freezing, NPs will be excluded from the ordered ice, increasing the local NP concentration and inducing aggregation (40, 41, 65). SEM images of P25 in 1 mM NaCl and either 0 or 10 ppm NOM after FT suggest that more and larger aggregates are formed in the presence of NOM than in the absence (Figure S5). Why this aggregation is either more pronounced or irreversible in the presence but not absence of NOM is unclear. The implication that NOM is associated with greater aggregation is somewhat counter to previous investigations that have shown that NOM helps to promote the disaggregation of NPs in stirred suspensions (7, 66, 67). However, the timescales associated with these effects are typically on the order of days to weeks, much longer than the timeframe required to prepare and begin conducting column experiments. Furthermore, NOM is generally associated with the formation of more open, less compact aggregates, as Chowdhury *et al.* demonstrate in presence of humic acid (68), but this does not take into account the forced proximity associated with freezing.

While bridging is possible in the presence of divalent cations (i.e., in MHRW suspensions), this phenomenon would be expected to also occur in 10C samples (69-71). Additionally, bridging does not explain the behavior in 1 mM NaCl where neither Ca^{2+} or Mg^{2+} ions are present. A possible explanation is related to the stresses that occur during the process of

freezing that have been shown to be capable of rupturing lipid bilayers and breaking apart polycaprolactone polymer NPs (42, 44, 72). Freezing natural waters containing dissolved organic matter appeared to change the conformation of various organic matter fractions (e.g., fulvic or humic fractions), as measured by changes in the spectrophotometric properties (73, 74). Increasing the number of FT cycles led to a greater decrease in fluorescence across a range of freshwater samples (75). Thus, the stresses associated with FT may be capable of altering or removing some of the organics from the NP surface, facilitating aggregation.

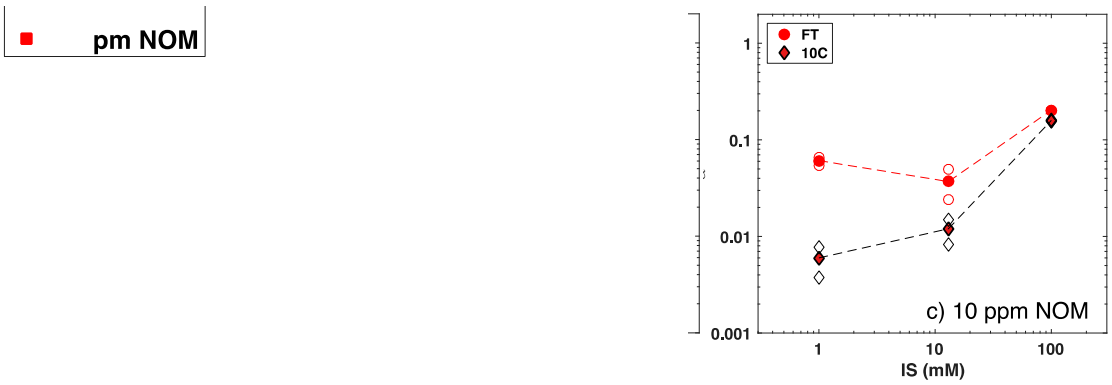

Figure 4. Stability diagrams showing attachment efficiency ($\alpha_{intensity}$) versus IS for P25 NPs exposed to either freeze-thaw (FT) or held at 10 °C for 24 h (10C) in the presence of a) 0 ppm NOM b) 1 ppm NOM and c) 10 ppm NOM. Filled icons are the average of duplicate measurements (open icons).

Figure 4 compares calculated α values for the two different 24 h pretreatments: FT samples (solid colored circles) versus 10C controls (colored diamonds outlined in black). As was the case for t0 samples, an increase in α was observed with increasing IS for both FT and 10C suspensions. No appreciable difference was observed in ZP values between 10C and FT samples for a given IS and NOM concentration (Table 2).

The broad trends of particle stability being enhanced in the presence of NOM are observed here as they were for t0 samples. In the absence of NOM (Figure 4a), similar α values are observed for both FT and 10C samples, with only a slight difference at 100 mM NaCl. These results suggest that in the absence of electrosteric stabilization, the extent of aggregation induced by the FT cycle is similar to what occurs when suspensions are kept at 10 °C for 24 h. For suspensions containing 1 and 10 ppm NOM (Figures 4b and 4c), freezing leads to an increase in α compared to the corresponding 10C controls. These differences are most pronounced at 1 mM NaCl, while α values for FT and 10C begin to converge as IS increases and particle stability decreases.

Table 2. Summary of NP characterization for FT and 10C suspensions. Apparent α values are calculated from intensity weighted sizes.

				Influent Aggregate Size (Diameter, nm)				Apparent α	
Suspension	**IS (mM)**	**NOM (ppm)**	**ZP (mV)**	**Z-average**	**PDI**	**Intensity Weighted**	C/C_0	**Z-average**	**Intensity Weighted**
P25, 10C	1	0	-30.3 ± 1.3	154	0.24	145	0.99	0.004	0.004
		1	-32.1 ± 2.0	149	0.23	162	0.99	0.005	0.006
		10	-34.8 ± 0.5	146	0.18	202	0.99	0.005	0.006
	MHRW (13)	0	-11.1 ± 0.3	1191	0.43	882	0.01	1.203	1.488
		1	-17.8 ± 0.1	163	0.22	157	0.89	0.013	0.012
		10	-22.1 ± 0.5	233	0.25	347	0.95	0.009	0.012
	100	0	-16.1 ± 2.4	2631	1.00	385	0.04	0.355	1.219
		1	-24.5 ± 0.6	701	0.36	608	0.45	0.307	0.305
		10	-23.5 ± 1.7	457	0.42	407	0.05	0.168	0.159
P25, FT	1	0	-30.3 ± 0.6	150	0.22	157	0.99	0.005	0.005
		1	-30.8 ± 1.2	4340	1.00	109	0.90	0.023	0.023
		10	-28.1 ± 0.3	2081	0.98	165	0.75	0.048	0.061
	MHRW (13)	0	-10.1 ± 0.6	1189	0.46	717	0.01	1.237	1.612
		1	-17.2 ± 1.6	495	0.54	157	0.82	0.060	0.028
		10	-16.2 ± 0.3	301	0.39	555	0.89	0.027	0.037
	100	0	-16.7 ± 0.5	4790	1.00	211	0.02	0.102	1.060
		1	-24.4 ± 1.1	784	0.32	603	0.36	0.450	0.453
		10	-21.5 ± 1.2	643	0.62	243	0.02	0.331	0.203

Interestingly, at low IS, the presence of NOM can lead to increased deposition after being exposed to a FT cycle. Aggregates in 1 mM NaCl post FT exhibit greater attachment in the presence of NOM than in the absence. This follows the observation of greater aggregate sizes for 1 and 10 ppm NOM suspensions in 1 mM NaCl (Figure 3a). BTCs indicate that both t0 and 10C suspensions have almost no retention (C/C_0 = 0.99 for both) while FT suspensions exhibit greater retention (C/C_0 = 0.75). A similar trend is observed for suspensions in MHRW and 1 ppm NOM, though the differences in both Z- average size and C/C_0 are less (Figure 3c). Figure 3b compares BTCs for 1 mM NaCl and 10 ppm NOM for FT, 10C, and t0 column tests. The BTCs for 10C and t0 are the same (C/C_0 = 0.99, 0.99, respectively), but the BTC for the same water chemistry subjected to FT is much lower (C/C_0 = 0.75). Comparing FT results for 1 mM NaCl, an increase in the calculated α is observed (Figure 4) with increasing NOM concentration, from 0 ppm (α = 0.005) to 1 ppm (α = 0.023) and 10 ppm NOM (α = 0.061). This increase in α with NOM concentration is not observed in 10C controls of the same samples (α = 0.004, 0.005, 0.004 for 0, 1, 10 ppm NOM, respectively). DLS measurements indicate that the Z-average size of FT suspensions (e.g., 2081 nm for 1 mM NaCl, 1 ppm NOM) is greater than 10C suspensions (146 nm) and t0 suspensions (188 nm) for these conditions (Figure 3a, Table 2). Additionally, larger aggregates are observed in FT suspensions compared to 10C suspensions in SEM images (Figure S5). This suggests that the observed variation in α in the presence of NOM may be associated with the deposition of large agglomerates that do not completely disassociate when the suspension is thawed. At less stable water chemistries (high IS, e.g., 0 ppm NOM, 100 mM NaCl), the relative importance of aggregate size is diminished as deposition is already favorable. Interestingly, for NPs

suspended in 1 mM NaCl and MHRW in the absence of NOM, no difference in the Z-average size is observed, in agreement with the similar α values.

3.4. Attachment Efficiency Depends on Particle Size

Given that all column tests were performed under the same conditions (i.e. at 10 °C), the impact of FT on TiO_2 NP transport in this study can be assigned to the induced aggregation. The greater Z-average size and PDI of aggregates from DLS measurements and the decrease in C/C_0 values after freezing in turn highlight the impact of size on NP retention and the associated calculations of α. This is also observed in t0 samples for CoRI aggregates that are larger and more polydisperse than P25 aggregates in the same water chemistry. Comparing BTCs for P25 and CoRI for a given water condition (representative curves shown in Figure S4), reduced transport is consistently observed for CoRI suspensions. Petosa *et al.* refer to their calculations of attachment efficiency as 'apparent α' to highlight that straining is a mechanism outside traditional colloid filtration theory that influences their results (28). Here, we take the same approach (Tables 1 & 2), acknowledging that the extent of retention, and consequently, the calculations of α may be influenced not only by Brownian motion, differential settling, and interception but also by additional mechanisms beyond what are considered in conventional transport theory (62, 63).

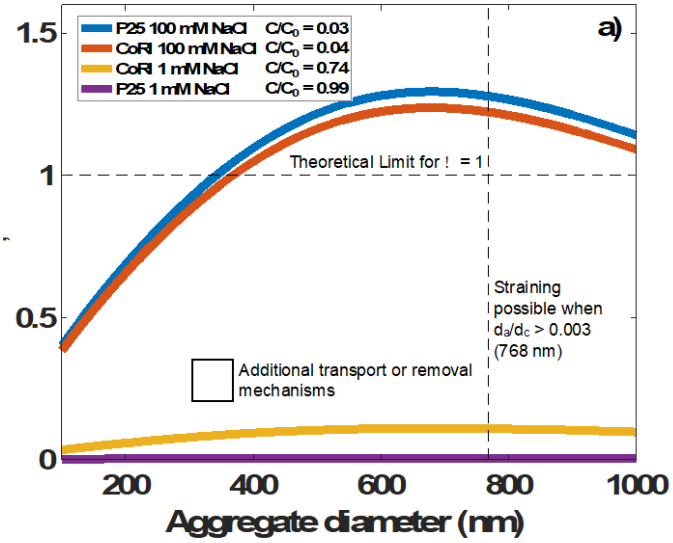
a)
P25 100 mM NaCl C/C0 = 0.03
CoRI 100 mM NaCl C/C0 = 0.04
CoRI 1 mM NaCl C/C0 = 0.74
P25 1 mM NaCl C/C0 = 0.99
Theoretical Limit for ! = 1
Straining possible when da/dc > 0.003 (768 nm)
Additional transport or removal mechanisms
1.5
1
0.5
0
200
400
600
800
1000
Aggregate diameter (nm)

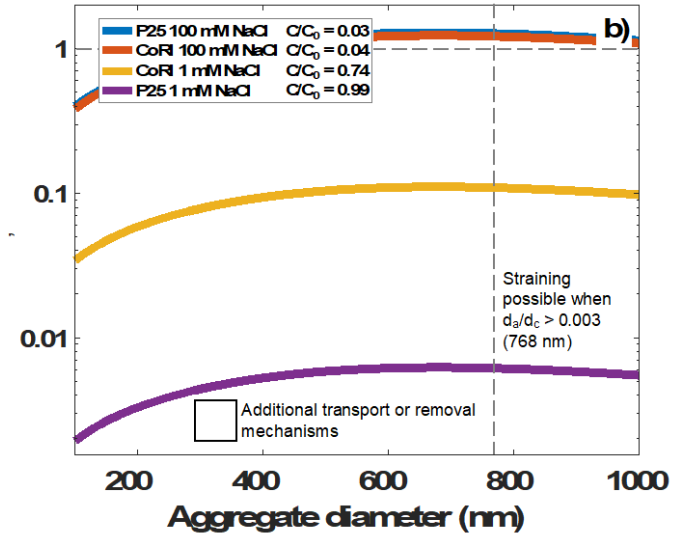
b)
P25 100 mM NaCl C/C0 = 0.03
CoRI 100 mM NaCl C/C0 = 0.04
CoRI 1 mM NaCl C/C0 = 0.74
P25 1 mM NaCl C/C0 = 0.99
Straining possible when da/dc > 0.003 (768 nm)
Additional transport or removal mechanisms
1
0.1
0.01
200
400
600
800
1000
Aggregate diameter (nm)

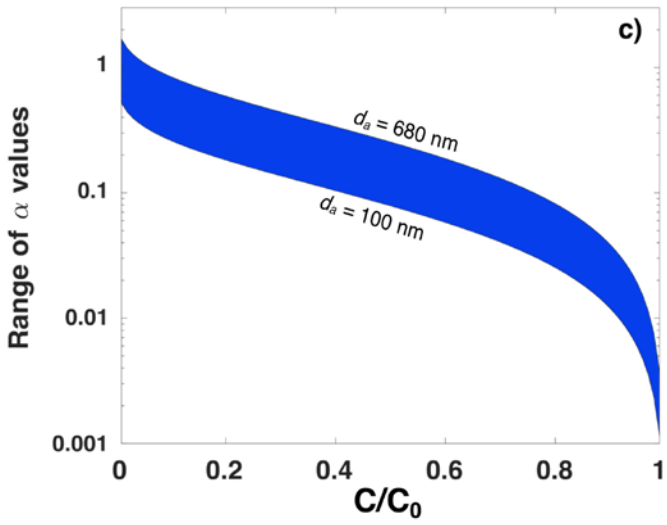

Figure 5. Theoretical α values versus aggregate diameter, calculated using C/C_0 measurements from four NP suspensions and shown on a) linear and b) log scales. Note for destabilized particles (100 mM NaCl), P25 and CoRI curves overlap on a log scale. c) Calculated α values versus C/C_0 as a function of aggregate diameter ranging from 100 – 768 nm.

However, for aggregate diameters small enough to readily fit through pores (i.e. < ~768 nm), complications still exist in calculating a single value for α. Results calculated from both the Z-average and intensity weighted sizes are reported in this work. As discussed in Section 3.2, $\alpha_{\text{z-avg}}$ is generally smaller than $\alpha_{\text{intensity}}$, and can vary quite significantly, (Figure S6). When NP transport through the column is low (e.g., P25 100 mM NaCl, C/C_0 =0.03) (Figure 5a), α depends greatly on size and can range from 0.400 – 1.3. As C/C_0 (and transport) increases (e.g., P25 1 mM NaCl, C/C_0 =0.99), the potential range of α becomes more limited (0.002 – 0.006). In relative terms, however, the range stays similar, leading to parallel curves when the same values are plotted on a log scale (Figure 5b).

These ranges in α arise from the single-collector contact efficiency (η_0), which depends on aggregate size and the physical experimental conditions (e.g., temperature, fluid and NP

densities, Hamaker constant, fluid approach velocity), rather than on the solution chemistry. Therefore, the values for η_0 as a function of aggregate size (Figure S6) are the same for all solution chemistries in this study. From Equation 1 we note that η_0 is inversely proportional to α. For the given conditions here at a fixed, measured value of C/C_0, the minimum in η_0 and, thus, maximum α value that can be calculated occurs for aggregates of ~680 nm (Figure 5a). Because η_0 depends on the diameter of the aggregate, if a distribution of sizes exists, the calculated α values will also have a distribution. This is shown in Figures 5a and 5b for C/C_0 values measured using both NPs in either 1 or 100 mM NaCl and the absence of NOM. When calculating the possible range of α values using a given column length and measured C/C_0, α values greater than the theoretical limit of 1 can be obtained. These correspond to situations in which the column conditions are insufficient to produce the measured deposition (C/C_0) without transport mechanisms beyond the conventional transport phenomena. Broadly, calculations that return α values greater than one suggest the presence of additional transport mechanisms beyond Brownian motion, interception, and gravitational sedimentation.

Because suspensions are often polydisperse, calculating a 'true α' falls victim to the same considerations of assigning an average aggregate size from DLS measurements. Figure 5c illustrates the range of α values that are possible under the current experimental conditions assuming aggregate sizes from 100 – 768 nm for a given C/C_0 value. The lower bound corresponds to aggregate sizes of 100 nm, while the upper bound is observed at ~680 nm, corresponding to the minimum in η_0 (Figure S6). When comparing heterogeneous suspensions, small variations in α may be attributable to distributions in size influencing the

single-collector contact efficiency as well as differences in potential energy barriers to attachment. Thus, more clear distinctions can be drawn between α values when the PDIs of suspensions are low. When the PDI of a measured suspension is large (e.g. CoRI t0 suspensions in this work), one should be more cautious about making distinctions between α values within the same order of magnitude. Small differences (less than an order of magnitude) in apparent α values between polydisperse suspensions may simply be a result of the aggregate size distribution.

3. Environmental Implications

Here, inherent differences in CoRI versus P25 NPs led to suspensions with dissimilar aggregate sizes and stabilities for the same water chemistry. Comparing between NP types, differences in aggregation impacted particle transport and calculations of α. Exposure to FT increased the size of aggregates compared to a 24 h pre-treatment at 10 °C, and resulted in higher α values. Freezing may also be capable of inducing stresses that influence the NOM coating around particles, leading to enhanced aggregation. The impact of freezing and the mechanisms that influence surface interactions in these cases are phenomena that deserve more attention. Recently, FT cycles were observed to induce particle release from painted surfaces (9) as well as increase biofilm formation in *Pseudomonas aeruginosa* (34). While a single FT cycle brought about significant aggregation for the TiO_2 NPs here, other NP types may be more or less stable in suspension. This work highlights that the aggregation and transport behavior of colloidal suspensions subjected to FT cycles, expected during late fall or early spring shoulder periods can differ from what would be expected during warmer months, which are often more represented by traditional column testing at a fixed, often

room, temperature. Recent models have attempted to describe the impact of aggregate size distributions on NP transport and highlight the complexity conferred by heterogeneity in environmental samples (76, 77). Future work should consider these differences to better understand the impact of climate change and winter conditions.

4. Acknowledgements

The authors acknowledge the financial support of the Canada Research Chairs program, the Natural Sciences and Engineering Research Council of Canada, Environment and Climate Change Canada, and the Coatings Research Institute. The authors thank L. M. Hernandez for her help with TEM and SEM. The authors also thank S. Ghoshal for helpful discussions.

5. References

1. Keller AA, Lazareva A. Predicted Releases of Engineered Nanomaterials: From Global to Regional to Local. Environmental Science & Technology Letters. 2014;1(1):65-70.
2. Piccinno F, Gottschalk F, Seeger S, Nowack B. Industrial production quantities and uses of ten engineered nanomaterials in Europe and the world. J Nanopart Res. 2012;14(9).
3. Keller AA, McFerran S, Lazareva A, Suh S. Global life cycle releases of engineered nanomaterials. J Nanopart Res. 2013;15(6):1-17.
4. Bossa N, Chaurand P, Levard C, Borschneck D, Miche H, Vicente J, et al. Environmental exposure to TiO2 nanomaterials incorporated in building material. Environmental pollution. 2017;220:1160-70.
5. Al-Kattan A, Wichser A, Vonbank R, Brunner S, Ulrich A, Zuin S, et al. Release of TiO 2 from paints containing pigment-TiO 2 or nano-TiO 2 by weathering. Environmental Science: Processes & Impacts. 2013;15(12):2186-93.
6. Shandilya N, Le Bihan O, Bressot C, Morgeneyer M. Emission of titanium dioxide nanoparticles from building materials to the environment by wear and weather. Environ Sci Technol. 2015;49(4):2163-70.
7. Baalousha M, Yang Y, Vance ME, Colman BP, McNeal S, Xu J, et al. Outdoor urban nanomaterials: the emergence of a new, integrated, and critical field of study. Sci Total Environ. 2016;557:740-53.
8. Lankone RS, Challis KE, Bi Y, Hanigan D, Reed RB, Zaikova T, et al. Methodology for quantifying engineered nanomaterial release from diverse product matrices under outdoor

weathering conditions and implications for life cycle assessment. Environmental Science: Nano. 2017;4(9):1784-97.
9. Azimzada A, Farner JM, Hadioui M, Liu-Kang C, Jreije I, Tufenkji N, et al. Release of TiO2 nanoparticles from painted surfaces in cold climates: characterization using a high sensitivity single-particle ICP-MS. Environmental Science: Nano. 2020.
10. Farner JM, Cheong RS, Mahé E, Anand H, Tufenkji N. Comparing TiO2 nanoparticle formulations: stability and photoreactivity are key factors in acute toxicity to Daphnia magna. Environmental Science: Nano. 2019.
11. Gottschalk F, Sonderer T, Scholz RW, Nowack B. Modeled environmental concentrations of engineered nanomaterials (TiO2, ZnO, Ag, CNT, fullerenes) for different regions. Environ Sci Technol. 2009;43(24):9216-22.
12. Mueller NC, Nowack B. Exposure modeling of engineered nanoparticles in the environment. Environ Sci Technol. 2008;42(12):4447-53.
13. Gondikas AP, Kammer Fvd, Reed RB, Wagner S, Ranville JF, Hofmann T. Release of TiO2 nanoparticles from sunscreens into surface waters: a one-year survey at the old Danube recreational Lake. Environ Sci Technol. 2014;48(10):5415-22.
14. Kiser M, Westerhoff P, Benn T, Wang Y, Perez-Rivera J, Hristovski K. Titanium nanomaterial removal and release from wastewater treatment plants. Environ Sci Technol. 2009;43(17):6757-63.
15. Reed R, Martin D, Bednar A, Montaño M, Westerhoff P, Ranville J. Multi-day diurnal measurements of Ti-containing nanoparticle and organic sunscreen chemical release during recreational use of a natural surface water. Environmental Science: Nano. 2017;4(1):69-77.
16. Tufenkji N, Ryan JN, Elimelech M. Peer reviewed: the promise of bank filtration. ACS Publications; 2002.
17. Tourinho PS, Van Gestel CA, Lofts S, Svendsen C, Soares AM, Loureiro S. Metal-based nanoparticles in soil: Fate, behavior, and effects on soil invertebrates. Environ Toxicol Chem. 2012;31(8):1679-92.
18. Fang J, Xu M-j, Wang D-j, Wen B, Han J-y. Modeling the transport of TiO2 nanoparticle aggregates in saturated and unsaturated granular media: effects of ionic strength and pH. Water Res. 2013;47(3):1399-408.
19. Slomberg DL, Ollivier P, Miche H, Angeletti B, Bruchet A, Philibert M, et al. Nanoparticle stability in lake water shaped by natural organic matter properties and presence of particulate matter. Sci Total Environ. 2019;656:338-46.
20. Petosa AR, Jaisi DP, Quevedo IR, Elimelech M, Tufenkji N. Aggregation and deposition of engineered nanomaterials in aquatic environments: role of physicochemical interactions. Environ Sci Technol. 2010;44(17):6532-49.
21. Sharma VK. Aggregation and toxicity of titanium dioxide nanoparticles in aquatic environment—a review. Journal of Environmental Science and Health Part A. 2009;44(14):1485-95.
22. Liu X, Chen G, Su C. Effects of material properties on sedimentation and aggregation of titanium dioxide nanoparticles of anatase and rutile in the aqueous phase. J Colloid Interf Sci. 2011;363(1):84-91.
23. Hotze EM, Phenrat T, Lowry GV. Nanoparticle Aggregation: Challenges to Understanding Transport and Reactivity in the Environment. J Environ Qual. 2010;39(6):1909-24.

24. Thio BJR, Zhou D, Keller AA. Influence of natural organic matter on the aggregation and deposition of titanium dioxide nanoparticles. J Hazard Mater. 2011;189(1-2):556-63.
25. Liu W, Sun W, Borthwick AG, Ni J. Comparison on aggregation and sedimentation of titanium dioxide, titanate nanotubes and titanate nanotubes-TiO2: Influence of pH, ionic strength and natural organic matter. Colloids and Surfaces A: Physicochemical and Engineering Aspects. 2013;434:319-28.
26. Chowdhury I, Cwiertny DM, Walker SL. Combined factors influencing the aggregation and deposition of nano-TiO2 in the presence of humic acid and bacteria. Environ Sci Technol. 2012;46(13):6968-76.
27. Ren M, Horn H, Frimmel FH. Aggregation behavior of TiO2 nanoparticles in municipal effluent: Influence of ionic strengthen and organic compounds. Water Res. 2017;123:678-86.
28. Petosa AR, Brennan SJ, Rajput F, Tufenkji N. Transport of two metal oxide nanoparticles in saturated granular porous media: role of water chemistry and particle coating. Water Res. 2012;46(4):1273-85.
29. Tufenkji N, Elimelech M. Correlation equation for predicting single-collector efficiency in physicochemical filtration in saturated porous media. Environ Sci Technol. 2004;38(2):529-36.
30. Chen G, Liu X, Su C. Distinct effects of humic acid on transport and retention of TiO2 rutile nanoparticles in saturated sand columns. Environ Sci Technol. 2012;46(13):7142-50.
31. Chowdhury I, Hong Y, Honda RJ, Walker SL. Mechanisms of TiO2 nanoparticle transport in porous media: Role of solution chemistry, nanoparticle concentration, and flowrate. J Colloid Interf Sci. 2011;360(2):548-55.
32. Henry HA. Soil freeze–thaw cycle experiments: trends, methodological weaknesses and suggested improvements. Soil Biology and Biochemistry. 2007;39(5):977-86.
33. Zhang Z, Wei M, Wenjie F, Donghui X, Xin H. Reconstruction of soil particle composition during freeze-thaw cycling: a review. Pedosphere. 2016;26(2):167-79.
34. Hakimzadeh A, Okshevsky M, Maisuria V, Déziel E, Tufenkji N. Exposure to Freeze–Thaw Conditions Increases Virulence of Pseudomonas aeruginosa to Drosophila melanogaster. Environ Sci Technol. 2018;52(24):14180-6.
35. Rocard JM, Asadishad B, Samonte PRV, Ghoshal S, Tufenkji N. Natural freeze-thaw cycles may increase the risk associated with Salmonella contamination in surface and groundwater environments. Water research X. 2018;1:100005.
36. Asadishad B, Olsson AL, Dusane DH, Ghoshal S, Tufenkji N. Transport, motility, biofilm forming potential and survival of Bacillus subtilis exposed to cold temperature and freeze–thaw. Water Res. 2014;58:239-47.
37. Asadishad B, Ghoshal S, Tufenkji N. Role of cold climate and freeze–thaw on the survival, transport, and virulence of Yersinia enterocolitica. Environ Sci Technol. 2013;47(24):14169-77.
38. Henry HA. Climate change and soil freezing dynamics: historical trends and projected changes. Climatic Change. 2008;87(3-4):421-34.
39. Mohanty SK, Saiers JE, Ryan JN. Colloid-facilitated mobilization of metals by freeze–thaw cycles. Environ Sci Technol. 2014;48(2):977-84.
40. Niu L, Panyam J. Freeze concentration-induced PLGA and polystyrene nanoparticle aggregation: Imaging and rational design of lyoprotection. Journal of Controlled Release. 2017;248:125-32.

41. Abdelwahed W, Degobert G, Stainmesse S, Fessi H. Freeze-drying of nanoparticles: formulation, process and storage considerations. Advanced drug delivery reviews. 2006;58(15):1688-713.
42. Alkilany AM, Abulateefeh SR, Mills KK, Bani Yaseen AI, Hamaly MA, Alkhatib HS, et al. Colloidal stability of citrate and mercaptoacetic acid capped gold nanoparticles upon lyophilization: effect of capping ligand attachment and type of cryoprotectants. Langmuir. 2014;30(46):13799-808.
43. Wang C, Chen X, Wang B, Huang M, Wang B, Jiang Y, et al. Freeze-casting produces a graphene oxide aerogel with a radial and centrosymmetric structure. Acs Nano. 2018;12(6):5816-25.
44. Zhang L, Li P, Li D, Guo S, Wang E. Effect of freeze− thawing on lipid bilayer-protected gold nanoparticles. Langmuir. 2008;24(7):3407-11.
45. Taurozzi J, Hackley V, Wiesner M. Preparation of a nanoscale TiO2 aqueous dispersion for toxicological or environmental testing. NIST Special Publication. 2012;1200:3.
46. Nobbmann U, Connah M, Fish B, Varley P, Gee C, Mulot S, et al. Dynamic light scattering as a relative tool for assessing the molecular integrity and stability of monoclonal antibodies. Biotechnology and genetic engineering reviews. 2007;24(1):117-28.
47. Hackley V, Clogston J. Measuring the size of nanoparticles in aqueous media using batch-mode dynamic light scattering. NIST special publication. 2007;1200:6.
48. Malvern I. Inform white paper dynamic light scattering. Malvern: Malvern Instruments Ltd. 2011:1-6.
49. Bhattacharjee S. DLS and zeta potential–What they are and what they are not? Journal of Controlled Release. 2016;235:337-51.
50. Stetefeld J, McKenna SA, Patel TR. Dynamic light scattering: a practical guide and applications in biomedical sciences. Biophysical reviews. 2016;8(4):409-27.
51. Nobbmann U, Morfesis A. Light scattering and nanoparticles. Materials Today. 2009;12(5):52-4.
52. EPA U. Methods for measuring the acute toxicity of effluents and receiving waters to freshwater and marine organisms. EPA/600/4-90; 1993.
53. Pelley AJ, Tufenkji N. Effect of particle size and natural organic matter on the migration of nano-and microscale latex particles in saturated porous media. J Colloid Interf Sci. 2008;321(1):74-83.
54. Loux NT, Savage N. An assessment of the fate of metal oxide nanomaterials in porous media. Water, air, and soil pollution. 2008;194(1-4):227.
55. Fatisson J, Domingos RF, Wilkinson KJ, Tufenkji N. Deposition of TiO2 nanoparticles onto silica measured using a quartz crystal microbalance with dissipation monitoring. Langmuir. 2009;25(11):6062-9.
56. Feiler A, Jenkins P, Ralston J. Metal oxide surfaces separated by aqueous solutions of linear polyphosphates: DLVO and non-DLVO interaction forces. Physical Chemistry Chemical Physics. 2000;2(24):5678-83.
57. Farner Budarz J, Turolla A, Piasecki AF, Bottero J-Y, Antonelli M, Wiesner MR. Influence of aqueous inorganic anions on the reactivity of nanoparticles in TiO2 photocatalysis. Langmuir. 2017;33(11):2770-9.

58. Derjaguin B, Landau L. The theory of stability of highly charged lyophobic sols and coalescence of highly charged particles in electrolyte solutions. Acta Physicochim URSS. 1941;14:633-52.
59. Verwey E, Overbeek JTG. Long distance forces acting between colloidal particles. Trans Faraday Soc. 1946;42:B117-B23.
60. Bradford SA, Torkzaban S, Walker SL. Coupling of physical and chemical mechanisms of colloid straining in saturated porous media. Water Res. 2007;41(13):3012-24.
61. Quevedo IR, Olsson AL, Clark RJ, Veinot JG, Tufenkji N. Interpreting deposition behavior of polydisperse surface-modified nanoparticles using QCM-D and sand-packed columns. Environ Eng Sci. 2014;31(7):326-37.
62. Babakhani P, Bridge J, Doong R-a, Phenrat T. Continuum-based models and concepts for the transport of nanoparticles in saturated porous media: A state-of-the-science review. Adv Colloid Interfac. 2017;246:75-104.
63. Liu D, Johnson PR, Elimelech M. Colloid deposition dynamics in flow-through porous media: Role of electrolyte concentration. Environ Sci Technol. 1995;29(12):2963-73.
64. Holzer M, Vogel V, Mäntele W, Schwartz D, Haase W, Langer K. Physico-chemical characterisation of PLGA nanoparticles after freeze-drying and storage. European Journal of Pharmaceutics and Biopharmaceutics. 2009;72(2):428-37.
65. Logsdon GS, Edgerley Jr E. Sludge dewatering by freezing. Journal (American Water Works Association). 1971:734-40.
66. Loosli F, Le Coustumer P, Stoll S. TiO 2 nanoparticles aggregation and disaggregation in presence of alginate and Suwannee River humic acids. pH and concentration effects on nanoparticle stability. Water Res. 2013;47(16):6052-63.
67. Omar FM, Aziz HA, Stoll S. Aggregation and disaggregation of ZnO nanoparticles: influence of pH and adsorption of Suwannee River humic acid. Sci Total Environ. 2014;468:195-201.
68. Chowdhury I, Walker SL, Mylon SE. Aggregate morphology of nano-TiO2: role of primary particle size, solution chemistry, and organic matter. Environ Sci: Processes Impacts. 2013;15(1):275-82.
69. Chen KL, Mylon SE, Elimelech M. Enhanced aggregation of alginate-coated iron oxide (hematite) nanoparticles in the presence of calcium, strontium, and barium cations. Langmuir. 2007;23(11):5920-8.
70. Zhang Y, Chen Y, Westerhoff P, Crittenden J. Impact of natural organic matter and divalent cations on the stability of aqueous nanoparticles. Water Res. 2009;43(17):4249-57.
71. Domingos RF, Peyrot C, Wilkinson KJ. Aggregation of titanium dioxide nanoparticles: role of calcium and phosphate. Environmental Chemistry. 2010;7(1):61-6.
72. Choi M, Briancon S, Andrieu J, Min S, Fessi H. Effect of freeze-drying process conditions on the stability of nanoparticles. Drying technology. 2004;22(1-2):335-46.
73. Spencer RG, Bolton L, Baker A. Freeze/thaw and pH effects on freshwater dissolved organic matter fluorescence and absorbance properties from a number of UK locations. Water Res. 2007;41(13):2941-50.
74. Xue S, Wen Y, Hui X, Zhang L, Zhang Z, Wang J, et al. The migration and transformation of dissolved organic matter during the freezing processes of water. Journal of Environmental Sciences. 2015;27:168-78.

75. Hudson N, Baker A, Reynolds DM, Carliell-Marquet C, Ward D. Changes in freshwater organic matter fluorescence intensity with freezing/thawing and dehydration/rehydration. Journal of Geophysical Research: Biogeosciences. 2009;114(G4).
76. Raychoudhury T, Tufenkji N, Ghoshal S. Aggregation and deposition kinetics of carboxymethyl cellulose-modified zero-valent iron nanoparticles in porous media. Water Res. 2012;46(6):1735-44.
77. Babakhani P. The impact of nanoparticle aggregation on their size exclusion during transport in porous media: One-and three-dimensional modelling investigations. Scientific reports. 2019;9(1):1-12.